https://doi.org/10.5194/egusphere-2026-5239
Preprint. Discussion started: 9 September 2026

Comparison of measurements from pressure-recording inverted echo sounders, moored ADCPs, and ocean reanalysis products in the North Equatorial Current region of the western Pacific

Yeeun Jang[1], Jae-Hun Park[2], Eung Kim[3], Chanhyung Jeon[1,4*]

[1]Department of Oceanography, Pusan National University, Busan, Republic of Korea
[2]Department of Ocean Sciences, College of Natural Sciences, Inha University, Incheon, Republic of Korea
[3]Marine Domain Research Division, Korea Institute of Ocean Science and Technology, Busan, Republic of Korea
[4]Marine Research Institute, Pusan National University, Busan, Republic of Korea

Correspondence to: Chanhyung Jeon (jeonc@pusan.ac.kr)

Abstract. With recent advances in data-assimilating ocean reanalysis products, mesoscale oceanic processes can be more realistically represented, increasing the need for regional performance assessments. Here, two widely used products, the Global Ocean Physics Reanalysis (GLORYS) and the Hybrid Coordinate Ocean Model reanalysis (HYCOM), are compared against two years of in situ observations from four pressure-recording inverted echo sounders (PIESs) and two acoustic Doppler current profilers (ADCPs) in the North Equatorial Current (NEC) region. While both products reproduce sea surface height (SSH) reasonably well, GLORYS shows closer agreement with the observations. However, their correlations are lower at the southern than at the northern sites located approximately 419 km apart, ranging from 0.84 (0.79) at the northernmost PIES site to 0.76 (0.76) at the southernmost site for GLORYS (HYCOM), consistent with the known degradation of satellite-measured SSH toward lower latitudes. The same trend also appears in the zonal current fields, with depth-averaged correlations (60–400 m) dropping far more sharply, from 0.75 (0.65) at the northern ADCP station to 0.36 (0.39) at the southern station. This degradation is largely associated with the reduced accuracy of satellite altimetry toward lower latitudes; assimilation of these errors can distort reanalysis SSH gradients and, consequently, zonal geostrophic currents. The relatively poor representation of intermediate-layer zonal currents at the southern ADCP station, particularly in GLORYS, may also reflect contributions from inaccuracies in the upper-ocean density structure. Although the accumulated density structure errors are comparable between the northern and southern NEC regions, differences in the relative contributions of the surface and baroclinic geostrophic components appear to explain the greater influence of baroclinic errors on the intermediate current in the southern region. In contrast, HYCOM shows vertically coherent anomalous flows throughout the water column, suggesting that surface-geostrophic variability is projected too deeply. Overall, GLORYS effectively reproduces the variability of the NEC region, though care should be taken of its limitations in interpreting intermediate-layer currents and variability affected by satellite altimetry errors, particularly in the southern NEC region.

https://doi.org/10.5194/egusphere-2026-5239
Preprint. Discussion started: 9 September 2026

1 Introduction

Recent advances in ocean reanalysis products have enabled the reproduction of spatiotemporally continuous, high-resolution oceanic fields that allow a more realistic representation of major mesoscale processes (Storto et al., 2019; Lellouche et al., 2021). Historically, ocean reanalysis products were primarily used to capture long-term climate variability, leveraging uniform numerical model configurations and consistent data assimilation frameworks. Due to their typical objectives and historical use, most assessments have been conducted at global to basin scales, to quantify uncertainties among products (Balmaseda et al., 2015; Masina et al., 2017; Storto et al., 2017; Storto et al., 2019). These assessments, however, often rely on datasets that are actively assimilated into the reanalysis systems themselves, including satellite altimetry, Argo float observations, and various in situ profile measurements. Such reliance is largely unavoidable, as independent observational datasets are indeed scarce in the open ocean, making robust evaluation particularly challenging.

Meanwhile, the latest generation of ocean reanalysis products is now provided at eddy-resolving resolutions (e.g., 1/12°). Researchers are increasingly utilizing these high-resolution products not only to investigate multi-annual variability (e.g., Zhong et al., 2021; Xia et al., 2022) but also to examine shorter variations associated with mesoscale processes (e.g., Song et al., 2023; Aristizábal Vargas et al., 2024). It has therefore become essential to assess the performance of ocean reanalysis products at specific regional scales of interest (e.g., Verezemskaya et al., 2021), as global scale comparisons may mask significant regional inaccuracies or discrepancies. Given that the primary strength of these eddy-resolving products lies in capturing mesoscale eddies and high-resolution current dynamics, regions characterized by energetic mesoscale variability and complex vertical current structures therefore provide useful testbeds for such regional evaluations.

The North Equatorial Current (NEC) region of the western Pacific is characterized by energetic mesoscale variability and a complicated structure of vertically sheared zonal currents (Fig. 1a). The meridional sea surface height (SSH, η) gradient between approximately 8–18° N supports the broad westward geostrophic NEC in this region (Fig. 1b; Qiu et al., 2015). This westward-flowing current occupies a wide meridional space and ultimately bifurcates into the Kuroshio and Mindanao currents after encountering the Philippine coast. Embedded within this wind-driven westward flow, the Subtropical Countercurrent (STCC) appears as a surface-intensified eastward flow near 19–21° N (Kobashi et al., 2006) and is associated with energetic mesoscale eddies generated through baroclinic instability (Qiu, 1999; Kobashi and Kawamura, 2002). Beneath the upper-layer system, the North Equatorial Undercurrent (NEUC) flows eastward below the thermocline, forming a distinct vertically sheared pattern with the surface-intensified westward NEC (Qiu et al., 2013; Zhang et al., 2017; Huang et al., 2022). This complex arrangement of alternating zonal currents and energetic mesoscale variability makes the NEC region particularly challenging to simulate, and therefore a suitable testbed for regional evaluation of ocean reanalysis products.

To evaluate the representation of the NEC region in ocean reanalysis products, we utilized an array of four pressure-recording inverted echo sounders (PIESs) and two subsurface moorings equipped with 75 kHz acoustic Doppler current profilers (ADCPs) (Fig. 1b). PIES observations have previously been used to estimate steric and mass-loading components of sea level variability and to validate satellite altimetry products (Baker-Yeboah et al., 2009; Park et al., 2012; Behnisch et al., 2013; Donohue et al.,

https://doi.org/10.5194/egusphere-2026-5239
Preprint. Discussion started: 9 September 2026

2016; Jeon et al., 2018; Hwang et al., 2021). Among these studies, Jeon et al. (2018) has demonstrated that satellite-derived SSH in the western Pacific is often contaminated by hump artifact errors (Dibarboure et al., 2014; CMEMS, 2026), which induced discrepancies exceeding 10 cm at multiple observation sites. Furthermore, the reduced agreement of satellite altimetry with in situ observations toward lower latitudes in the western Pacific raises concerns that such altimetric errors may be introduced into ocean reanalysis products through data assimilation.

Two years of continuous measurements from six moorings provide an independent dataset for assessing the performance of major ocean reanalysis products and to examine the effects of satellite altimetry errors in these products. Section 2 describes the observational datasets (PIES, ADCP, and in situ profiles), the configurations of the two reanalysis products – GLORYS and HYCOM – and the methodologies applied. Comparison results of sea level anomaly (SLA, η') and zonal currents are presented in Sect. 3. Section 4 discusses possible factors contributing to the zonal current discrepancies, focusing on SSH errors, regional background flow dynamics, and model-related thermohaline structures. Finally, Sect. 5 summarizes the key findings and concludes the study.

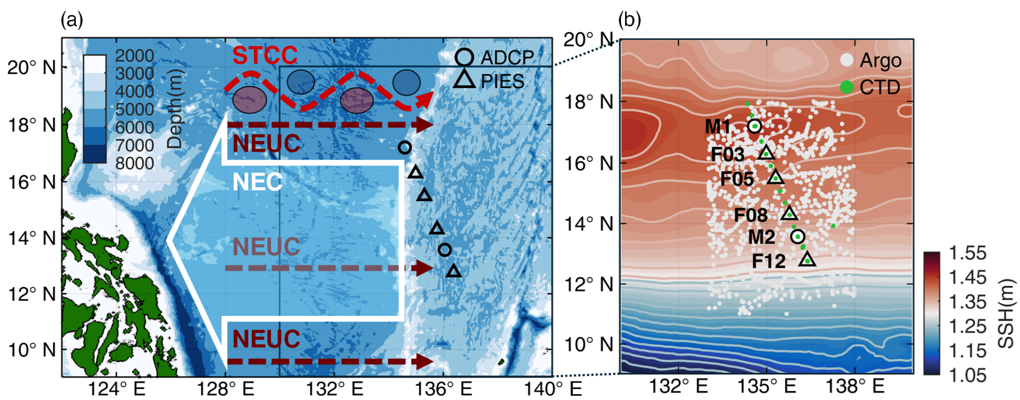

Figure 1: Locations of the mooring array and a schematic of the current system. (a) Schematic of the major current systems and bathymetry of the North Equatorial Current (NEC) region. The white-outlined, semi-transparent arrow represents the westward-flowing NEC that dominates most of the study region. Eastward currents are indicated by red dashed arrows: the Subtropical Countercurrent (STCC) and the North Equatorial Undercurrent (NEUC), with the latter shown in darker red as it flows beneath the NEC. (b) Locations of the four pressure-recording inverted echo sounder (PIES) sites (F03, F05, F08, and F12; triangles), the two subsurface mooring stations equipped with 75 kHz ADCPs (M1 and M2; circles), and the Argo and shipboard CTD profiles (grey and green dots, respectively) collected during the PIES observation period within 11–18° N, 133–138° E. The background map shows the absolute dynamic topography (ADT) averaged over the study period, with contours at 0.02 m intervals.

https://doi.org/10.5194/egusphere-2026-5239
Preprint. Discussion started: 9 September 2026

2 Data and methods

2.1 Observational datasets

A mooring array consisting of four PIESs and two ADCPs was deployed along the satellite altimeter track in the NEC region from June 2012 to May 2014, with station spacing increasing toward lower latitudes (Fig. 1b). The PIESs recorded acoustic round-trip travel time (τ) and bottom pressure (P_{bot}) using 10 min burst sampling (Jeon et al., 2023). These records are subsequently detided, 3-day low-pass filtered, and subsampled at 12 h intervals (Park et al., 2012; Donohue et al., 2016; Andres et al., 2020).

The τ is primarily sensitive to first-mode baroclinic variability (Watts and Rossby, 1977), and P_{bot} measures changes in the total mass overhead, the steric (baroclinic) and mass-loading (barotropic) components of the sea level change can be estimated from τ and P_{bot}, respectively (Baker-Yeboah et al., 2009; Park et al., 2012; Behnisch et al., 2013; Donohue et al., 2016; Jeon et al., 2018; Hwang et al., 2021). Following these established methods, steric and mass-loading components were derived and summed to obtain the total sea level change (η_{PIES}). In this region, the total variability is dominated by the baroclinic component, which contributes a variance 17 times larger than the barotropic component of sea level change on average (Jeon et al., 2018). The estimated total RMS error is 6.3 cm, and this accounts for the uncertainties in the conversion of τ to geopotential height using historical hydrocasts, and the minor contributions from pressure drift and tidal residuals. The detailed methodology for calculating each component, as well as the measurement accuracy of the PIES-equipped sensors, is described in Jeon et al. (2018).

Subsurface moorings at M1 and M2 were equipped with upward-looking 75 kHz RDI ADCPs at 460–470 m depth to record upper-layer currents from June 2012 to May 2014. The ADCPs provided hourly current profiles with a 10 m vertical bin. Measurements above 60 m and below 400 m were excluded due to large errors arising from backscattering noise near the sea surface and missing or unreliable measurements, respectively. Thus, we analyzed the zonal current component within the 60–400 m depth range after applying a 3-day low-pass filter and daily averaging.

The Argo program consists of a global array of autonomous profiling floats that provide continuous measurements of ocean temperature and salinity versus pressure, from the sea surface to 2000 dbar (Roemmich et al., 2019). Although Argo observations are assimilated into most modern reanalysis products and are therefore not strictly independent for validation, they remain a good resource for assessing the vertical thermohaline structures. In this study, delayed-mode temperature and salinity profiles near the observation sites (11–18° N, 133–138° E) were used to evaluate the thermohaline structures represented by the reanalyses (Fig. 1b, grey dots).

Additionally, a total of 57 CTD profiles were obtained during the shipboard observations of RV *Onnuri* in June 2012, May 2013, and May 2014, which also included the deployment and recovery of the four PIESs and two subsurface ADCPs used in this study. Of these, 41 profiles within the study domain (11–18° N, 133–138° E) were used to provide an independent estimate of the discrepancies between the observations and the reanalyses (Fig. 1b, green dots).

https://doi.org/10.5194/egusphere-2026-5239
Preprint. Discussion started: 9 September 2026

We used the delayed-time all-satellite altimeter gridded product produced and distributed by the Copernicus Marine Service (CMEMS, 2025). The product provides absolute dynamic topography (ADT) and absolute surface geostrophic currents on a 1/8° regular grid for the period 1993–2025. For the sea level comparison, satellite SLA (η'_{Sat}) was calculated by removing the time-mean during the PIES observation period (June 2012–May 2014). As the agreement between PIES and satellite altimetry in this region has already been evaluated by Jeon et al. (2018), the satellite SLA was included here as an additional reference to examine whether the reanalysis SLAs more closely follow the PIES observations or satellite-derived variability, and whether characteristic satellite errors are also reflected in the reanalysis products. The absolute surface geostrophic currents (u_{Sat}) provided by the product were used for comparison with the observed and reanalysis zonal currents at the M1 and M2 ADCP sites.

2.2 Ocean reanalysis products

The Global Ocean Physics Reanalysis (GLORYS12V1, hereafter GLORYS) is an eddy-resolving physical ocean reanalysis product provided by CMEMS (CMEMS, 2018), covering the satellite altimetry era from 1993 to the present (Lellouche et al., 2021). Based on the Nucleus for a European Model of the Ocean (NEMO) platform and driven by European Centre for Medium-Range Weather Forecasts (ECMWF) ERA-Interim atmospheric forcing, it jointly assimilates satellite data (along-track SLA, sea surface temperature, and sea ice) and in situ T/S profiles using a reduced-order Kalman filter with a 7-day assimilation cycle. The long-term bias of temperature and salinity data is adjusted by a 3D-VAR scheme with a one-month time scale. GLORYS has a horizontal resolution of 1/12° and 50 vertical levels structured by z-coordinates, with 22 levels located within the upper 100 m and spacing gradually increasing with depth (Lellouche et al., 2018, 2021).

The Global Ocean Forecast System 3.1 reanalysis, based on the Hybrid Coordinate Ocean Model (hereafter HYCOM), provides 3-hourly data with a horizontal resolution of 1/12° and 40 vertical layers (HYCOM Consortium, 2026). HYCOM is forced by National Centers for Environmental Prediction (NCEP) Climate Forecast System Reanalysis (CFSR) and Climate Forecast System Version 2 (CFSv2). Data assimilation is performed via the Navy Coupled Ocean Data Assimilation (NCODA; Cummings, 2005) system, which applies a 3D-VAR scheme in a daily update cycle to assimilate satellite altimetry, SST, and in situ profiles from XBTs, CTDs, and Argo floats. One unique feature of HYCOM is its hybrid vertical coordinate system, which smoothly transitions between isopycnic coordinates in the stratified open ocean, z-level coordinates in the mixed layer, and terrain-following sigma coordinates in shallow coastal regions (Chassignet et al., 2009). HYCOM specifically features 41 vertical layers (and interpolated to 40 standard levels), with at least the top 14 layers acting as sigma-z levels within the upper 84 m to provide enhanced resolution of the mixed layer and subsurface structure (Metzger et al., 2017). Since HYCOM provides 3-hourly data, all variables were used after applying 3-day low-pass filtering and daily averaging.

https://doi.org/10.5194/egusphere-2026-5239
Preprint. Discussion started: 9 September 2026

2.3 Methods

SLA from the four datasets (η'_{PIES}, η'_{Sat}, and two η'_{Re}s) was compared after removing their respective time-mean over the PIES observation period (Fig. 2). As the Dynamic Atmospheric Correction (DAC) is applied to the satellite altimetry product to remove high-frequency signals driven by atmospheric pressure and wind forcing (CMEMS, 2026), equivalent atmospheric and barotropic corrections were applied to the PIES measurements to ensure consistent comparisons among η'_{PIES}, η'_{Sat}, and η'_{Re}. Specifically, the DAC-derived pressure was removed from the PIES P_{bot} to obtain the mass-loading component of η_{PIES}, while τ was corrected for free surface displacements induced by mass-loading and the inverse barometer response prior to calculating the steric component (Park et al., 2012; Jeon et al., 2018). The exact conversion process is described in detail in Jeon et al. (2018).

We examined the vertical density structures of the reanalysis products to assess their potential contribution to baroclinic current errors by comparing temperature, salinity, and geopotential height (Z) profiles with those derived from Argo float and shipboard CTD observations. During the PIES observation period, a total of 998 temperature and salinity (T/S) profiles were obtained from the Argo program within the study domain (11–18° N, 133–138° E). Only delayed-mode profiles spanning from at least 60 dbar to 1000 dbar were used, with their temporal coverage broadly distributed throughout the observation period (not shown). To examine the discrepancies in reanalysis density structure within the NEC-dominant region, we focused on 510 profiles located south of 15° N (Fig. 8h); for the STCC–NEC alternating region, we used the remaining 488 profiles located north of 15° N (Fig. 9h). For the ship-based CTD profiles, 22 were located north of 15° N and 19 south of 15° N. Reanalysis profiles were spatially and temporally interpolated to the time and location of in situ profiles for direct comparison. We then calculated the geopotential height (Z, m) by:

$$Z = \frac{1}{g}\int_{p}^{0} \frac{1}{\rho(p)}\, dp, \tag{1}$$

for all four datasets, where p is a target pressure level, ρ is density, and g (= 9.8 m s^{-2}) is the gravitational acceleration.

The absolute geostrophic current referenced to altimetry (u_{abs}) can be decomposed into an absolute surface geostrophic current (u_{sfc}) and a baroclinic geostrophic current (u_{bc}):

$$u_{\text{abs}} = u_{\text{sfc}} + u_{\text{bc}}. \tag{2}$$

Here, u_{sfc} is derived from the ADT gradient provided by CMEMS and remains constant throughout the water column, while u_{bc} is obtained by integrating geopotential height from the target pressure to the surface. Thus, the zonal component of the absolute geostrophic current at a specific depth is expressed as:

$$u_{\text{sfc}} = -\frac{g}{f}\frac{\partial \eta}{\partial y},\; u_{\text{bc}} = -\frac{g}{f}\frac{\partial Z}{\partial y}, \tag{3}$$

$$u_{\text{abs}} = -\frac{g}{f}\frac{\partial \eta}{\partial y} - \frac{g}{f}\frac{\partial Z}{\partial y}, \tag{4}$$

https://doi.org/10.5194/egusphere-2026-5239
Preprint. Discussion started: 9 September 2026

where f is the Coriolis parameter. The discrepancies between reanalysis and observations were expressed using double-prime notation:

$$u''_{\mathrm{abs}} = u_{\mathrm{abs}}^{\mathrm{Re}} - u_{\mathrm{abs}}^{\mathrm{Obs}}. \tag{5}$$

To examine the impact of SSH gradient discrepancies on reanalysis zonal current at station M2, the cross-site difference, $\Delta\eta = \eta^{\mathrm{F12}} - \eta^{\mathrm{F08}}$, was calculated (Fig. 7a), as station M2 is located between PIES sites F08 and F12 (at a meridional distance of approximately 170 km; see Fig. 1). The PIES-derived SSH at sites F08 and F12 was determined by adding the time-mean ADT from satellite altimetry to the PIES-derived SLA (η'), thereby aligning it to the same reference level as ADT. Accordingly, a positive $\Delta\eta$ indicates an eastward flow, and a negative $\Delta\eta$ indicates the opposite. Although the oblique orientation of the PIES array along the Jason-2 track 214 limits the accurate estimation of the zonal component, it remains adequate for characterizing the dominant variability patterns, which are primarily zonal in this region (Zhang et al., 2017; Azminuddin et al., 2019).

For clarity, the notations introduced are summarized as follows: the prime (′) denotes the temporal anomaly relative to the time mean (e.g., SLA); the double prime (″) denotes the difference between reanalysis and observational data (observation − reanalysis, or reanalysis − observation); and the Δ denotes the spatial difference between two stations (e.g., $\Delta\eta = \eta^{\mathrm{F12}} - \eta^{\mathrm{F08}}$).

3 Results

3.1 Sea level anomaly (SLA, η')

Figure 2 shows SLAs of four datasets: PIES, satellite altimetry, GLORYS, and HYCOM. Consistent with the energetic mesoscale variability of the NEC region, all four datasets exhibit frequent sea-level up-and-downs throughout the observation period. Notably, from October to November 2013, both reanalyses successfully represented the significant sea-level drops triggered by consecutive typhoon passages (Jeon et al., 2022).

Among the reanalysis products, GLORYS showed higher correlations and smaller differences, exhibiting closer agreement with both η'_{PIES} and η'_{Sat} (Fig. 2). While HYCOM also showed a comparably high SLA reproducibility, it exhibited intermittent mismatches, particularly at F03 and F05 in February 2013 and across F03 to F08 from January to April 2014, resulting in larger RMSDs. These intermittent mismatches are discussed further in Sect. 4 in relation to the known noisy SSH issue in the Philippine Sea.

Consistent with η'_{Sat}, the correlations for both η'_{Re}s decreased toward lower latitudes in the order of F05 > F03 > F08 > F12. This latitudinal decline in performance suggests that the inaccuracies in satellite altimetry can degrade sea level representation in reanalysis products, raising concerns about inducing spurious geostrophic currents in this low-latitude region.

Mismatches (>0.1 m) are noticeably observed during February 2013 (at F03, F05, and F12), May–July 2013, and January–April 2014 across almost all sites in both η'_{Re}s and η'_{Sat}. The shadings in Fig. 2 indicate periods when satellite altimetry is contaminated by the hump artifact error (Dibarboure et al., 2014; Jeon et al., 2018), which also seems to induce spurious

https://doi.org/10.5194/egusphere-2026-5239
Preprint. Discussion started: 9 September 2026

variability in η'_{Re}. These errors, arising from irregularities in radar backscatter and primarily driven by rain cells, can induce spurious sea-level anomalies exceeding 0.1 m, which is more than three times the maximum error of global gridded SLA products (approximately 3 cm; CMEMS, 2026). During the shaded periods, η'_{Sat} and η'_{Re}s show closer agreement with each other than with η'_{PIES}. Given that reanalyses typically assimilate available satellite altimetry, this close agreement indicates that the hump artifact errors present in the satellite data are introduced into η'_{Re}, as noted by Jeon et al. (2018). Notably, HYCOM exhibits larger and more frequent mismatches than GLORYS. Most of these mismatches in HYCOM follow the trend of η'_{Sat} but some exceed 0.2 m, suggesting a substantial contribution from model-intrinsic variability beyond hump errors. Mismatches in GLORYS are moderately smaller than those in HYCOM but generally follow the variability of η'_{Sat}, indicating that the influence of hump errors remains.

https://doi.org/10.5194/egusphere-2026-5239
Preprint. Discussion started: 9 September 2026

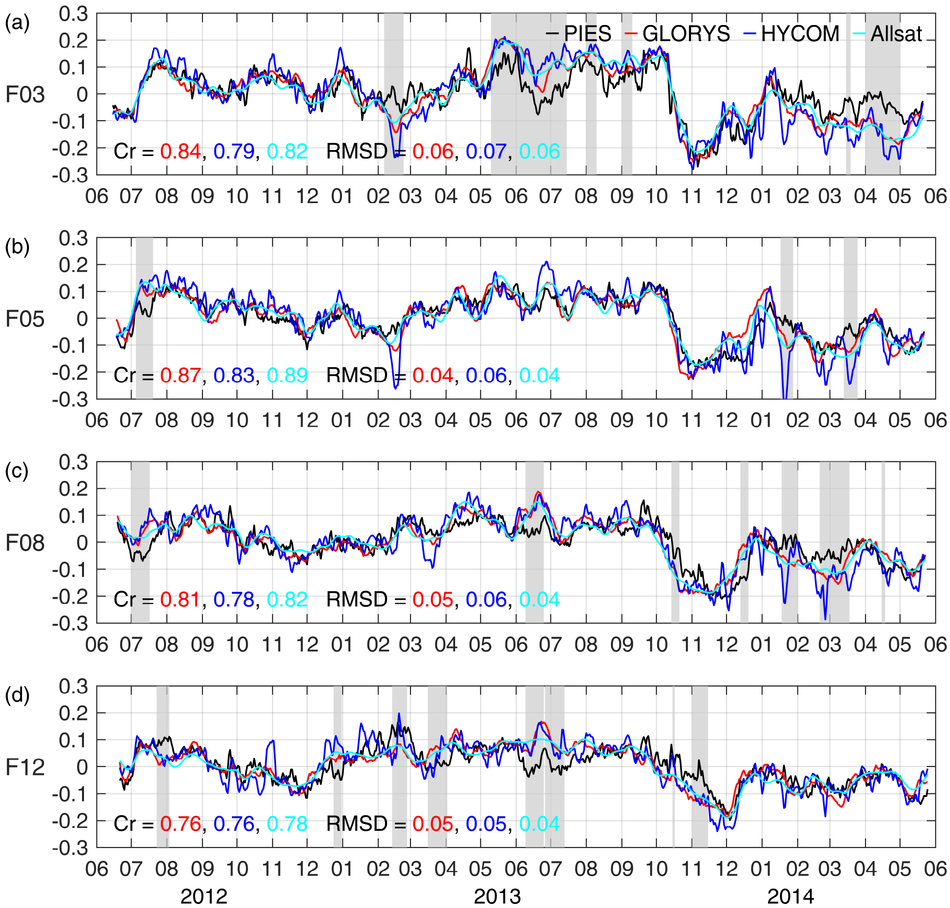

Figure 2: Time series of η'_{PIES} (black), η'_{Re} of GLORYS (red) and HYCOM (blue), and η'_{Sat} (cyan) at four PIES sites (F03, F05, F08, and F12). Correlation coefficients (Cr) and root-mean-squared differences (RMSD) between η'_{PIES} and each of η'_{Re} and η'_{Sat} are shown in the bottom-left corner of each panel, with colors matching their corresponding lines. Grey shadings denote periods of prominent discrepancies (> 0.1 m), where both η'_{Re}s and η'_{Sat} differ from η'_{PIES}.

3.2 Zonal current distribution

Figure 3 presents time-mean velocity profiles of two ADCPs from 60 to 400 m. The vertical structure from the ADCP at M1 (17.2° N) shows a reversal in zonal flow direction, reflecting the transition from a surface-intensified eastward STCC to a

https://doi.org/10.5194/egusphere-2026-5239
Preprint. Discussion started: 9 September 2026

dominant westward NEC below the thermocline (Zhang et al., 2017; Azminuddin et al., 2019; Huang et al., 2022). The mean zonal current of the STCC appears relatively weak, as its flow is intermittently modulated by energetic mesoscale eddies, resulting in a standard deviation that significantly exceeds its average (Qiu, 1999). In contrast, ADCP measurements at station M2 (13.6° N) were dominated by the NEC, representing a stable and significant westward flow extending to 400 m depth. Given that the time-mean meridional component is almost zero and the regional current system is mainly characterized by these alternating zonal jets, we decided to compare the zonal current of reanalyses rather than full velocity vectors.

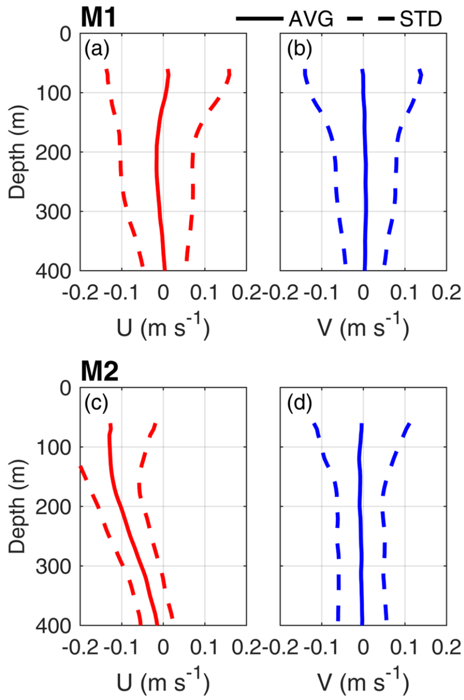

Figure 3: Vertical distributions of time-mean zonal (red) and meridional (blue) currents from mooring ADCPs at M1 and M2 during June 2012–May 2014. Solid and dashed lines denote the average (AVG) and standard deviation (STD), respectively.

Time series of zonal velocity profiles at M1 (M2) from ADCP, GLORYS, and HYCOM are represented in Fig. 4 (5), with the profiles of correlation coefficients between u_{ADCP} and each of u_{Sat}, u_{GLORYS}, and u_{HYCOM}. Each station represents a distinct vertical zonal velocity structure as previously shown in Fig. 3. As captured by ADCPs, station M1 is characterized by shifting upper-layer zonal currents, which are primarily dominated by the surface-intensified STCC and NEC, except for one NEUC extension event from October to November 2012 (Fig. 4a). In contrast, station M2 features a structure dominated by the westward-flowing NEC, which is intermittently influenced by the eastward-flowing NEUC extending upward from the deeper layers (Fig. 5a; Azminuddin et al., 2019).

https://doi.org/10.5194/egusphere-2026-5239
Preprint. Discussion started: 9 September 2026

The satellite-derived absolute surface geostrophic zonal current shows relatively high correlations with the ADCP currents in the upper layer (60–150 m), with the highest correlation at 60 m, suggesting a strong influence of the surface geostrophic component on upper-layer current variability (Fig. 4d). At station M1, vertically averaged correlation coefficients with ADCP are 0.75 for GLORYS and 0.65 for HYCOM. GLORYS shows the highest correlations in the subsurface layer (150–250 m) and maintains consistently good agreement throughout the water column (Fig. 4e). HYCOM, however, shows comparable correlations in the upper layer (60–180 m) but shows a nearly linear decrease with increasing depth (Fig. 4f).

During the observation period, both reanalysis products successfully reproduced the STCC-dominant phase observed by ADCP at station M1 (Fig. 4a–c). GLORYS smoothly represents the reversal of STCC and NEC and the vertical distribution of flow intensity that is stronger in the upper layers and weaker with depth, resulting in relatively high correlations within the whole water column (Fig. 4e). Despite its overall high performance, GLORYS occasionally fails to capture the variations in the STCC–NEC system. For instance, from June to July 2013, GLORYS simulates a strong westward flow throughout the observed water column, whereas the ADCP observes an eastward flow (Fig. 4a, b). This discrepancy overlaps with when hump errors occurred at F03 with elevated SLA in GLORYS (Fig. 2a). However, elevated SLA at F03 relative to northern M1 enhances the southward sea level gradient ($\frac{\partial \eta}{\partial y} < 0$), which geostrophically induces a spurious eastward current anomaly ($u > 0$, Eq. (3)). Nonetheless, this mismatch does not exclude a broader influence of hump errors, because their spatially variable distribution can alter the assimilated SSH gradients around M1 (Jeon et al., 2018). The resulting spatial gradients in the assimilated SLA field may introduce geostrophic current biases that do not necessarily align with the expected direction of the error. HYCOM also exhibits anomalous westward current in July 2013 (Fig. 4c), suggesting that the discrepancies originate from the identical error source.

HYCOM showed its highest correlation within the upper layer (60–180 m), yet its excessive short-term temporal variability and overly linear representation of vertical intensity led to higher RMSD and lower correlations in the intermediate layer (180–400 m) (Fig. 4f). Overall, GLORYS reproduces the alternating zonal jets and the abrupt velocity gradient at approximately 150 m reasonably well, which contributes to the high correlation observed below the upper layer at station M1 (Fig. 4e).

https://doi.org/10.5194/egusphere-2026-5239
Preprint. Discussion started: 9 September 2026

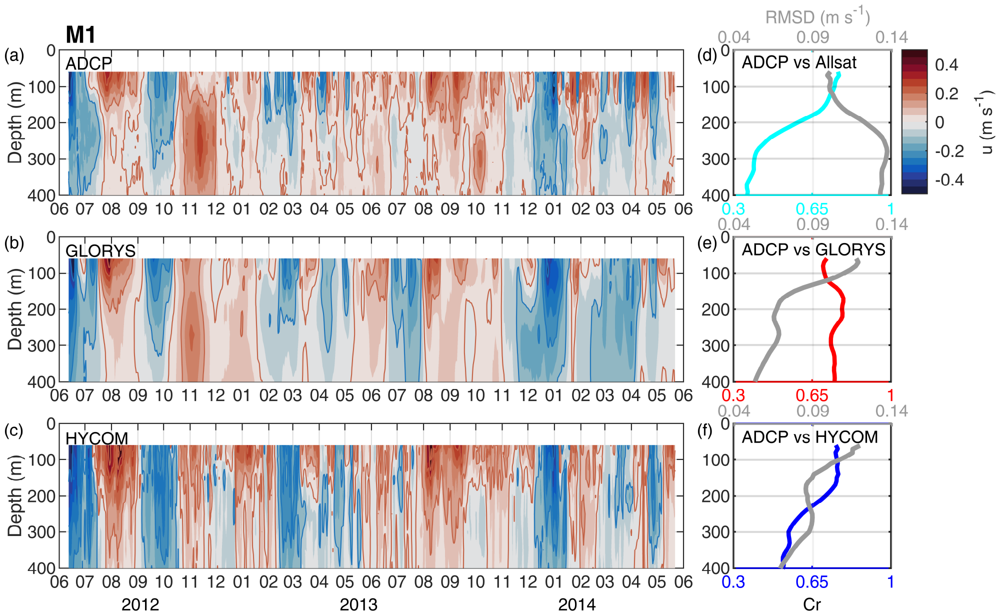

Figure 4: Comparison of vertical zonal velocity (*u*) structures at station M1. (a–c) Vertical distributions at M1 from (a) ADCP, (b) GLORYS, and (c) HYCOM. Contours range from –0.5 to 0.5 m s⁻¹ with 0.1 m s⁻¹ intervals. (d–f) Vertical profiles of Cr (colored lines) and RMSD (grey lines) at M1 between ADCP measurements and (d) satellite-derived surface geostrophic current (u_{Sat}), (e) GLORYS, and (f) HYCOM.

The prevailing westward flow at M2 is effectively captured in the zonal velocity fields of both GLORYS and HYCOM during the observation period (Fig. 5a–c). The high correlation between ADCP and satellite altimetry within the 60–150 m depth range indicates that the upper-layer flow in this region is largely geostrophic (Fig. 5d). Within this upper layer (60–150 m), GLORYS successfully resolves the subsurface variability of the NEC, with correlations ranging from 0.58 to 0.63, while HYCOM shows somewhat lower correlations of about 0.5 to 0.54 (Fig. 5e, f).

Below this layer, however, the two products show markedly different behavior. GLORYS does not reproduce the upward-penetrating NEUC in February and October–November 2013 (Fig. 5b), and this absence lowers its correlation and raises its RMSD within the intermediate layer (150–400 m) (Fig. 5e). HYCOM, in contrast, overly reproduces the NEUC, simulating anomalous eastward flows throughout the entire water column in the same period. As a result, HYCOM's correlation is already lower in the upper layer and remains relatively low but stable through the intermediate layer (Fig. 5f), while GLORYS exhibits a more rapid decline in correlation within the intermediate layer.

https://doi.org/10.5194/egusphere-2026-5239
Preprint. Discussion started: 9 September 2026

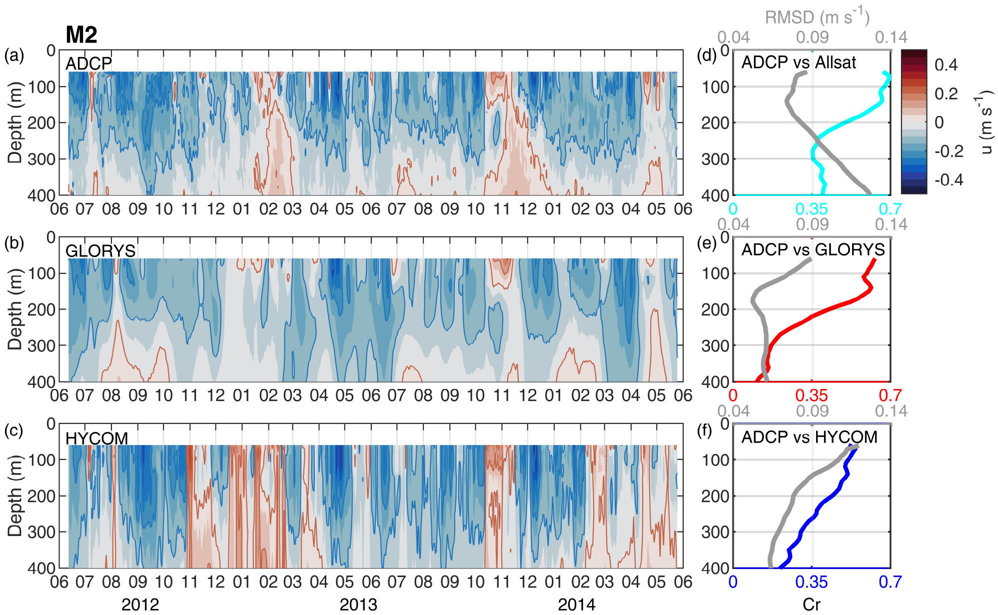

Figure 5: Same as Fig. 4, but for station M2.

Again, the mean correlation coefficients with ADCPs are 0.75 (0.65) at station M1 and 0.36 (0.39) at station M2 in GLORYS (HYCOM), which reveals the same latitudinal decline in performance (M1 > M2) as the SLA comparison (F05 > F03 > F08 > F12). Possible effects from erroneous SSH must be considered when interpreting geostrophic currents. Moreover, the complexity of the errors in zonal currents suggests that factors beyond SSH contamination are involved. The differences in regional background dynamics and reanalysis characteristics could induce distinct patterns of zonal velocity errors, raising the need for additional analysis. The plausible factors and their implications will be discussed in detail in Sect. 4.

4 Discussion

While both reanalysis products successfully reproduce SLA, they show lower performance in capturing zonal velocity at the NEC-dominant site, M2, compared to M1. This lower correlation highlights limitations in the representation of zonal currents over the southern NEC region. Rather than a single source, this diminished performance likely stems from a compound effect of several factors, including the potential influence of satellite-altimetry errors through data assimilation, regional differences in background-flow dynamics, and model characteristics and configurations. Among these, satellite altimetry errors are particularly notable: performance degrades toward low latitudes in the western Pacific (Fig. 2), where the error magnitude of hump artifact events can become comparable to or even exceed real SSH variations (Jeon et al., 2018).

https://doi.org/10.5194/egusphere-2026-5239
Preprint. Discussion started: 9 September 2026

The first two empirical orthogonal function (EOF) modes explain more than 90 % of the total zonal-current variance at both M1 and M2 in all datasets, indicating that they capture the dominant vertical structures of current variability (Fig. 6). At M1, the ADCP observations are characterized by relatively simple, surface-intensified variability, which is reasonably reproduced by both GLORYS and HYCOM (Fig. 6a, b). In contrast, the observed variability at M2 exhibits a more vertically sheared and depth-dependent structure. In particular, EOF mode 1 shows a pronounced change in vertical gradient near the thermocline (~150 m), while EOF mode 2 displays stronger subsurface curvature and shear between approximately 150 and 300 m (Fig. 6c, d). These features indicate that the zonal current variability at M2 involves more vertically complex, higher-order structures than at M1, consistent with the previously reported complex baroclinic structure in the southern NEC region (Zhang et al., 2017; Huang et al., 2022).

The two reanalyses differ markedly in their ability to reproduce this enhanced vertical complexity at M2. HYCOM exhibits an overly coherent EOF1 structure, with considerably weaker shear than observed across the thermocline (Fig. 6c). Such excessive vertical coherence suggests that surface-intensified variability is projected too deeply into the water column, consistent with the spurious eastward flows extending toward the intermediate layer in Fig. 5c. GLORYS, in contrast, reproduces a stronger vertical gradient across the thermocline and therefore better captures the observed separation between upper-ocean and subsurface variability. Nevertheless, its subsurface structure remains weak, particularly in EOF mode 2, where the pronounced ADCP shear between 150 and 300 m is substantially underestimated (Fig. 6d). This underestimation is consistent with the weakened representation of NEUC variability at M2 shown in Fig. 5b.

https://doi.org/10.5194/egusphere-2026-5239
Preprint. Discussion started: 9 September 2026

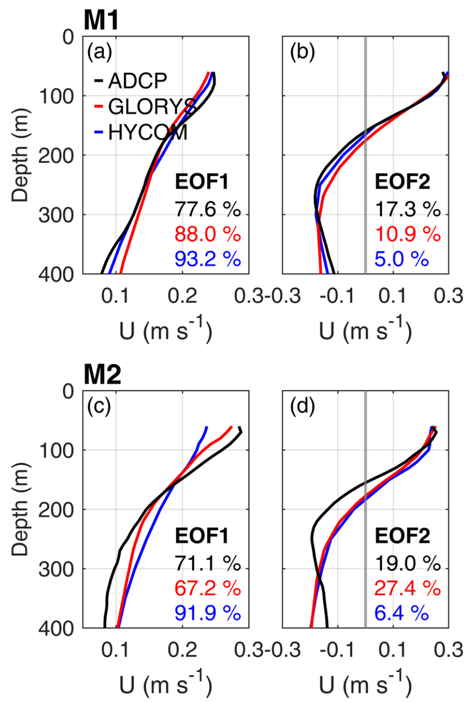

Figure 6: First and second EOF modes of the zonal velocity ($m\ s^{-1}$) time series at M1 (a, b) and M2 (c, d) within 60–400 m. Black, red, and blue lines represent EOF modes of ADCP, GLORYS, and HYCOM, respectively. The variance contribution (%) of each mode is indicated in the bottom-right of each panel.

Figure 7 compares the SSH difference between F12 and F08, $\Delta\eta = \eta^{\mathrm{F12}} - \eta^{\mathrm{F08}}$, calculated from PIES, GLORYS, and HYCOM, with the reanalysis zonal current differences ($u'' = u_{\mathrm{Re}} - u_{\mathrm{ADCP}}$) at station M2, where positive $\Delta\eta$ indicates eastward flow tendency. Comparison suggests that satellite-altimetry errors, including hump artifacts, can be reflected in reanalysis SSH gradients, $\Delta\eta$, and thereby contribute to anomalous geostrophic currents.

In GLORYS, zonal current discrepancies tend to occur when $\Delta\eta$ differs between PIES and GLORYS, particularly during periods affected by hump errors identified in Fig. 2. This tendency is evident in the negative and positive current anomalies observed in July and December 2012, respectively, both confined to the upper layer (60–150 m), as well as in January 2014, when a positive $\Delta\eta$ discrepancy coincided with erroneous eastward flows extending from the upper to intermediate layers (60–400 m) (Fig. 7a, b). The remaining zonal current errors in GLORYS are predominantly concentrated within the intermediate layer (150–400 m), without a clear concurrent signal in the upper layer. Three prominent intermediate-layer error events occurred in September 2012, February 2013, and October–December 2013, with the first event coinciding with an overestimated NEUC, whereas the latter two corresponded to an underrepresentation of the NEUC (Fig. 7b).

https://doi.org/10.5194/egusphere-2026-5239
Preprint. Discussion started: 9 September 2026

In HYCOM, consistent with the SLA comparisons (Fig. 2c, d), highly variable $\Delta\eta$ is closely associated with periods of anomalous zonal currents (Fig. 7a, c). For instance, the abrupt down-and-up fluctuations in $\Delta\eta$ from October to early November 2012 coincided with spurious westward-then-eastward u'' anomalies extending throughout the water column (Fig. 7c). These features are from vertically coherent horizontal flows simulated in HYCOM, which are consistent with the monotonically decreasing vertical structure of its primary EOF mode accounting for 91.9 % of the total variance (Fig. 6c). This pattern suggests that surface-intensified variability is projected too deeply into the water column, appearing as excessive upward penetration of the NEUC during November 2012–January 2013 and an overestimation of the NEC intensity during November–December 2013.

Overall, Fig. 7 indicates that errors in the SSH gradient contribute to the degraded representation of zonal currents in both reanalyses, although their vertical error patterns differ substantially. In particular, the intermediate-layer discrepancies and poor representation of the NEUC cannot be fully explained by SSH errors alone, suggesting an additional contribution from errors in the baroclinic component associated with the underlying upper-ocean density structure.

https://doi.org/10.5194/egusphere-2026-5239
Preprint. Discussion started: 9 September 2026

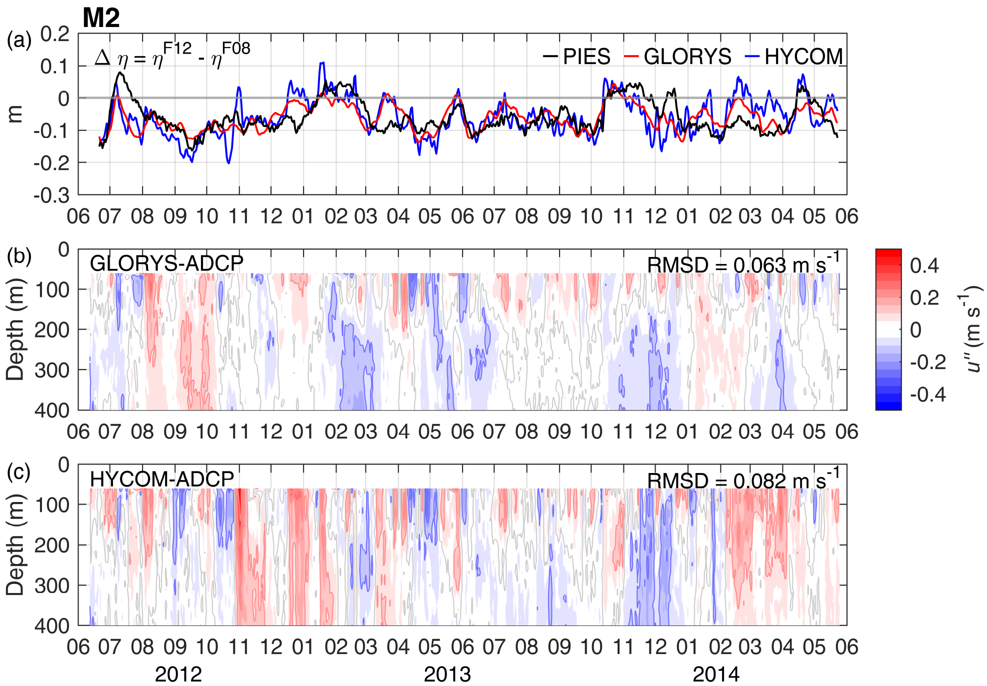

340 **Figure 7: Comparisons of observed and reanalysis-derived signals at station M2. (a) SSH difference (m) between sites F12 and F08 ($\Delta\eta = \eta^{F12} - \eta^{F08}$). (b, c) Vertical distributions of zonal currents difference ($u'' = u_{Re} - u_{ADCP}$) at station M2 for (b) GLORYS and (c) HYCOM, with colors ranging from −0.5 to 0.5 m s⁻¹ with 0.1 m s⁻¹ intervals same as Figs. 4 and 5. Depth-averaged root-mean-squared differences (RMSD) between u_{Re} and u_{ADCP} are shown in the top-right corner of each panel.**

Figures 6 and 7 show that both GLORYS and HYCOM struggle to simulate EOF2 zonal current variability, particularly that associated with the NEUC. Because errors in density structures in the upper ocean accumulate in geopotential height and can affect the baroclinic geostrophic component, we assessed the vertical profiles of GLORYS and HYCOM averaged over the NEC-dominant region (11–15° N, 133–138° E), which encompasses the M2 site. Figure 8 presents a comparison of temperature, salinity, and geopotential height profiles between observations and reanalysis products, with geopotential height calculated using Eq. (1). While the time-mean temperature, salinity, and geopotential height profiles from Argo, CTD, GLORYS, and HYCOM appear broadly similar when overlaid (Fig. 8a, c, e), the corresponding mean difference (observation − reanalysis) profiles reveal substantial discrepancies that could contribute to erroneous baroclinic currents.

In the subsurface layer (150–300 m), relatively large temperature discrepancies are found in both GLORYS and HYCOM (Fig. 8b). For salinity, larger discrepancies occur within the upper 200 m, slightly larger in HYCOM (Fig. 8d). These temperature and salinity discrepancies lead to corresponding errors in the geopotential height (Fig. 8f). Consequently, the discrepancy in

https://doi.org/10.5194/egusphere-2026-5239
Preprint. Discussion started: 9 September 2026

the vertical gradient of the geopotential height exhibits two distinct peaks at approximately 90 m and 160 m, primarily associated with salinity and temperature anomalies, respectively (Fig. 8g). The cumulative effect of these upper-ocean density errors causes the geopotential height discrepancies to increase rapidly below approximately 150 m in both products (Fig. 8f). When compared with the profiles from Argo assimilated into the reanalysis systems, both HYCOM and GLORYS exhibit geopotential height discrepancies of comparable magnitude, despite some differences between the two products. This similarity suggests that the accumulated upper-ocean density errors may also contribute to u_{bc} errors of broadly comparable magnitude in HYCOM and GLORYS.

However, because Argo profiles are assimilated into the reanalysis systems, evaluations based on Argo may underestimate discrepancies in density and geopotential height, and the subsequently associated baroclinic discrepancies. To address this potential bias, we additionally used independent shipboard CTD profiles that were not assimilated into the reanalyses, although their temporal coverage was limited compared to Argo. The time-mean differences between the independent CTD observations and the reanalysis products are within the standard-deviation range of the Argo-reanalysis differences (solid and dashed black lines in Fig. 8b, d, f, g). This independent comparison supports the overall magnitude and vertical pattern of the density-related errors estimated from the Argo-based analysis.

With the meridional distance between F08 and F12 (approximately 170 km), geopotential height discrepancies of 0.023–0.034 m (0.004–0.045 m when the standard deviations are considered) at 400 m depth (Fig. 8f) would correspond to an order-of-magnitude baroclinic current error of approximately 0.039–0.057 m s^{-1} (0.007–0.075 m s^{-1} when the standard deviations are considered). These values are of a comparable order of magnitude to the RMSDs of u'' for GLORYS and HYCOM at M2 (0.063–0.082 m s^{-1}) (Fig. 7b, c). Although errors in satellite-derived SSH, including the reduced correlations and hump errors, also contribute to the current discrepancies, this comparison suggests that accumulated errors in upper-ocean geopotential height may make a non-negligible contribution to intermediate-layer current errors through the baroclinic component.

https://doi.org/10.5194/egusphere-2026-5239
Preprint. Discussion started: 9 September 2026

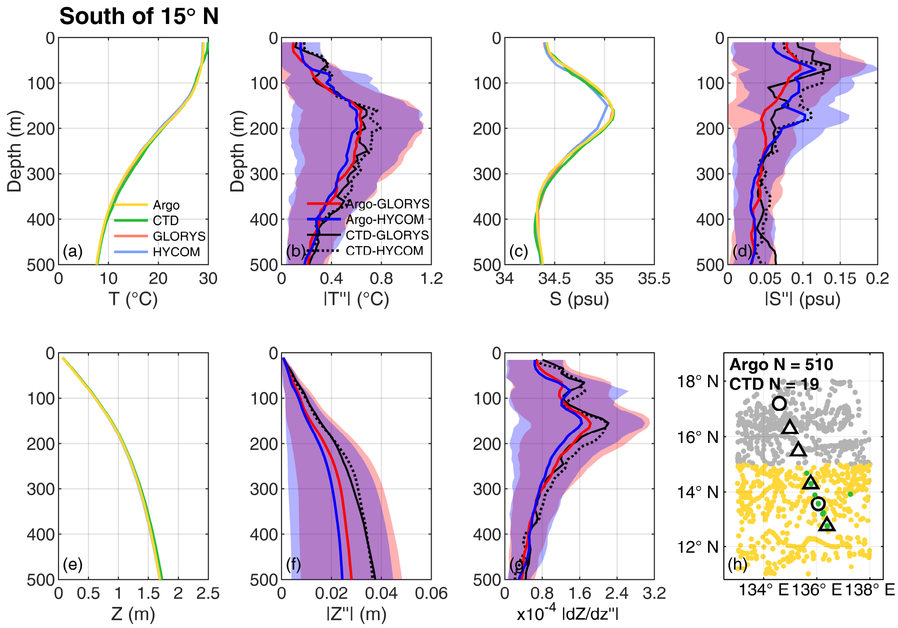

Figure 8: Comparison of vertical structures between reanalysis products and in situ profiles. Panels (a), (c), and (e) show the time-mean profiles of temperature (*T*), salinity (*S*), and geopotential height (*Z*), respectively, derived from Argo floats (yellow), shipboard CTD (green), GLORYS (pink), and HYCOM (sky blue). Panels (b), (d), (f), and (g) show the time-mean profiles of the absolute differences in temperature ($|T''|$), salinity ($|S''|$), geopotential height ($|Z''|$), and the vertical gradient of geopotential height ($|\frac{dZ''}{dz}|$), respectively, between the in situ and reanalysis profiles: Argo − GLORYS (red), Argo − HYCOM (blue), CTD − GLORYS (black), and CTD − HYCOM (dashed black). Red and blue shaded areas denote the standard deviation ranges of the Argo − GLORYS and Argo − HYCOM differences. (h) Locations of the in situ profiles collected during the PIES observation period within 11–18° N, 133–138° E (grey dots), with profiles south of 15° N highlighted in yellow for Argo and in green for shipboard CTD.

Given that the correlation between ADCP and reanalysis zonal currents is higher at M1 than at M2, we conducted the same analysis for the northern domain of the study region (15–18° N, 133–138° E), which encompasses the M1 site, where the STCC and NEC alternate, to examine whether geopotential height discrepancies similarly accumulate and contribute to baroclinic current errors (Fig. 9). Although temperature discrepancies are more broadly distributed with depth in the northern domain and the salinity discrepancies also differ somewhat in vertical structure, the geopotential-height gradient discrepancy exhibits a less pronounced peak than in the southern domain (Fig. 9b, d, g). Nonetheless, the overall pattern is similar to that in the southern domain around M2: the integrated effect of upper-ocean density errors increases with depth, leading to larger geopotential height discrepancies below approximately 150 m (Fig. 9f). Indeed, the accumulated geopotential height discrepancies at the intermediate depths are comparable between the two regions, reaching approximately 0.027 m at 400 m

https://doi.org/10.5194/egusphere-2026-5239
Preprint. Discussion started: 9 September 2026

(red lines in Figs. 8f and 9f), whereas the associated intermediate-layer current errors are substantially larger at M2 than at M1, particularly in GLORYS.

Despite comparable geopotential height discrepancies, the contrasting current responses between M1 and M2 appear to be primarily related to the different relative contributions of the surface and baroclinic geostrophic components. The stronger meridional SSH gradient in the northern domain produces a larger surface geostrophic current at M1, with u_{Sat} ranging from −0.39 to 0.40 m s^{-1}, compared with −0.35 to 0.11 m s^{-1} at M2. Indeed, the standard deviations of u_{Sat} and 60 m u_{ADCP} at M1 are 0.14 and 0.15 m s^{-1}, respectively, but noticeably smaller at M2 (0.09 and 0.11 m s^{-1}, respectively). Consequently, errors in the baroclinic component constitute a relatively smaller fraction of the total current variability at M1. At M2, in contrast, the weaker surface geostrophic component allows accumulated baroclinic errors to more strongly affect the intermediate-layer current.

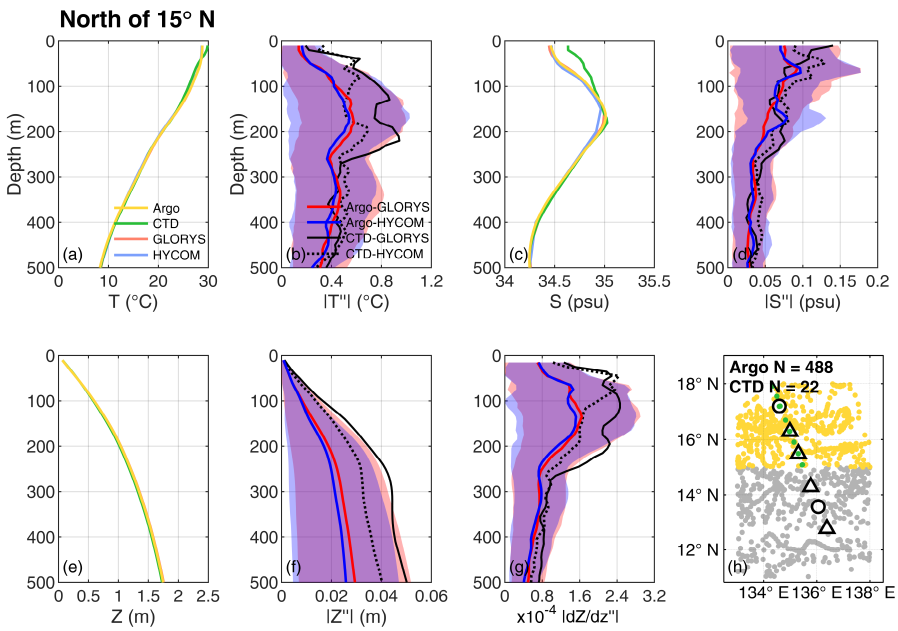

Figure 9: Same as Fig. 8, but for profiles north of 15° N (highlighted in yellow and green).

Beyond the regional differences discussed above, GLORYS and HYCOM also exhibit distinct vertical structures in their zonal current errors (Fig. 7b, c). HYCOM shows more vertically coherent current anomalies that are closely associated with variations in SSH, whereas the error in GLORYS is more pronounced in the intermediate layer, where the baroclinic component becomes relatively important.

A known noisy sea surface problem has been reported for HYCOM in the Philippine Sea (HYCOM Consortium, 2026), which may contribute to the enhanced short-term variability and relatively large RMSDs in both SLA and zonal currents. One plausible source is thermobaric instability (TBI), a known numerical artifact in HYCOM that can arise under weak stratification and excessively thick isopycnal layers (Hallberg, 2005). Recent HYCOM experiments show that limiting layer thickness substantially reduces the associated numerical noise (Abdulfatai et al., 2026, submitted), and TBI has also been suggested as a possible explanation for the noisy behavior in the Philippine Sea (A. Wallcraft, personal communication, 2026), although its contribution cannot be directly assessed in this paper.

Other differences between GLORYS and HYCOM may also be relevant to the contrasting error structures. For instance, HYCOM uses the NCODA system with a daily assimilation cycle, whereas GLORYS applies a 7-day assimilation cycle together with a longer-time scale temperature and salinity bias correction (Metzger et al., 2017; Lellouche et al., 2021). The two products also use different vertical coordinate systems, which could influence the representation of vertical thermohaline structure and associated baroclinic currents. However, because the two reanalyses differ in several aspects, including numerical model formulation, atmospheric forcing, vertical coordinates, and data assimilation frameworks, the influence of individual factors cannot be quantified here.

5 Summary and conclusion

We compared two widely used ocean reanalysis products, GLORYS and HYCOM, with time series data from four PIES and two ADCP stations, in the NEC region of the western Pacific. PIES-derived SLAs calculated from τ and P_{bot}, zonal currents from ADCPs, as well as various in situ profiles allowed us to assess the performance of reanalysis products in the NEC region. SLA of reanalysis products was successfully aligned with PIES-derived SLAs, with average correlation coefficients of 0.82 for GLORYS and 0.79 for HYCOM. Though their performance in reproducing SLA was robust, both products showed degrading correlations toward lower latitudes (F05 > F03 > F08 > F12), which coincided with the same latitudinal degradation seen in satellite altimetry. Previous studies have reported that satellite-measured SSH in this region exhibits hump artifact errors and lower agreement with observations toward the southern NEC region (Dibarboure et al., 2014; Jeon et al., 2018). Together, these findings suggest that satellite-altimetry-induced errors can be reflected in reanalysis SSH fields through data assimilation; specifically, GLORYS closely matched η'_{Sat}, whereas HYCOM simulated even more frequent spurious peaks.

The zonal current system in this region, consisting of the NEC, STCC, and NEUC (see Sect. 1), was observed by the ADCPs at stations M1 and M2. Station M1 is characterized by surface-intensified NEC and STCC switching, whereas station M2 is dominated by the NEC with intermittent NEUC penetration (Figs. 4 and 5). Although both products demonstrate comparable SLA agreements, their zonal velocity performance differs substantially, with depth-averaged correlations (60–400 m) decreasing from 0.75 (0.65) at M1 to 0.36 (0.39) at M2 for GLORYS (HYCOM). This abrupt latitudinal degradation in zonal currents is associated with SSH errors in the southern NEC region (Fig. 7), but the lowered correlation within the intermediate

https://doi.org/10.5194/egusphere-2026-5239
Preprint. Discussion started: 9 September 2026

layer at M2 and the corresponding poor representation of the NEUC suggest an additional contribution from inaccuracies in the upper-ocean density structure.

Even though GLORYS has a better capacity to reproduce sub-thermocline variability than HYCOM, particularly at M2 (Fig. 6c, d), it still exhibits spurious intermediate-layer currents that are more pronounced at M2 (Fig. 7). Although the estimated thermohaline structure errors are comparable between the northern and southern NEC regions, their influence on the intermediate-layer currents can differ because of the relative contributions of the surface and baroclinic geostrophic components. The northern NEC region shows a stronger dominance of u_{sfc} over u_{bc}, reducing the relative contribution of errors in u_{bc} to the total current. In the southern region, the weaker u_{sfc} allows comparable errors in u_{bc} to have a greater influence on the intermediate-layer current (150–400 m). In contrast, HYCOM represents more vertically coherent current anomalies that closely follow anomalous SSH variability, suggesting that surface-geostrophic variability is projected too deeply into the water column.

The continuous two-year mooring observations provided an opportunity not only to validate ocean reanalysis products but also to investigate the possible causes of discrepancies in the reanalysis products from the observations. Our findings support the concern noted by Jeon et al. (2018) that the hump artifact errors and the degradation of satellite-derived SSH toward lower latitudes can be reflected in reanalysis SSH and current fields through data assimilation. Therefore, it is crucial to be aware of satellite altimetry errors in the low-latitude western Pacific, as these errors degrade performance in both satellite altimetry and reanalysis products. While uncertainties persist in the intermediate zonal currents, GLORYS demonstrates a robust capacity to reproduce sea level and zonal current variability. GLORYS therefore appears suitable for investigating surface and upper-ocean variability in this region, although intermediate-layer zonal currents, particularly in the southern NEC region, should be interpreted with care.

Data availability

PIES-derived SSH data can be downloaded from https://github.com/PADOLab1/NEC_PIES. The subsurface ADCP and shipboard CTD data used in this study were provided by the Northwestern Pacific Ocean Study on Environment and Interactions between Deep Ocean and Marginal Seas (POSEIDON) project, KIOST. These data are not publicly available due to institutional reasons but can be accessed by researchers upon reasonable request via restricted access (Jeon and Azminuddin, 2018; https://doi.org/10.5281/zenodo.1228158). Argo float profiles (Argo, 2000) can be obtained from the Euro-Argo data selection service (https://dataselection.euro-argo.eu/). The all-satellite altimeter gridded product (ADT and absolute geostrophic velocity) and the GLORYS12V1 data are distributed through the Copernicus Marine Service (https://data.marine.copernicus.eu/product/SEALEVEL_GLO_PHY_L4_MY_008_047/services) and (https://data.marine.copernicus.eu/product/GLOBAL_MULTIYEAR_PHY_001_030/services), respectively. The HYCOM GOFS3.1 reanalysis is provided by the HYCOM Consortium (https://www.hycom.org/data/glbv0pt08/expt-53ptx).

Author contributions

YJ and CJ contributed to the conceptualization of this paper. YJ conducted the formal analysis and visualization, and wrote the original draft. CJ carried out the in situ observations, acquired funding, and edited previous versions of the manuscript. J-HP and EK carried out the in situ observations and contributed to the discussions. All authors reviewed the manuscript and approved the submitted version.

Competing interests

The authors declare that they have no conflict of interest.

Financial support

This work was supported by Korea Institute of Marine Science & Technology Promotion (KIMST) funded by the Ministry of Oceans and Fisheries, Korea, under grants RS-2023-00256330 (Development of risk managing technology tackling ocean and fisheries crisis around Korean Peninsula by Kuroshio Current) and RS-2022-KS221667 (Study on Northwestern Pacific Warming and Genesis and Rapid Intensification of Typhoon), and by National Research Foundation of Korea (NRF) under grant RS-2025-00522594.

https://doi.org/10.5194/egusphere-2026-5239
Preprint. Discussion started: 9 September 2026

References

Abdulfatai, M. A., Buijsman, M. C., Wallcraft, A. J., Arbic, B. K., and Shriver, J. F.: The impact of barotropic nudging on surface and internal tides in realistically-forced global ocean simulations, Ocean Model., submitted, 2026.

Andres, M., Musgrave, R. C., Rudnick, D. L., Zeiden, K. L., Peacock, T., and Park, J.-H.: On the predictability of sea surface height around Palau, J. Phys. Oceanogr., 50, 3267–3294, https://doi.org/10.1175/JPO-D-19-0310.1, 2020.

Argo: Argo float data and metadata from Global Data Assembly Centre (Argo GDAC), SEANOE [data set], https://doi.org/10.17882/42182, 2000.

Aristizábal Vargas, M. F., Kim, H.-S., Le Hénaff, M., Miles, T., Glenn, S., and Goni, G.: Evaluation of the ocean component on different coupled hurricane forecasting models using upper-ocean metrics relevant to air–sea heat fluxes during Hurricane Dorian (2019), Front. Earth Sci., 12, 1342390, https://doi.org/10.3389/feart.2024.1342390, 2024.

Azminuddin, F., Jeon, D., and Shin, C.-W.: Intraseasonal-to-interannual variability of the upper-layer zonal currents in the tropical northwest Pacific Ocean, Ocean Sci. J., 54, 15–27, https://doi.org/10.1007/s12601-019-0001-2, 2019.

Baker-Yeboah, S., Watts, D. R., and Byrne, D. A.: Measurements of sea surface height variability in the eastern South Atlantic from pressure sensor-equipped inverted echo sounders: baroclinic and barotropic components, J. Atmos. Ocean. Technol., 26, 2593–2609, https://doi.org/10.1175/2009JTECHO659.1, 2009.

Balmaseda, M. A., Hernandez, F., Storto, A., Palmer, M. D., Alves, O., Shi, L., Smith, G. C., Toyoda, T., Valdivieso, M., Barnier, B., Behringer, D., Boyer, T., Chang, Y.-S., Chepurin, G. A., Ferry, N., Forget, G., Fujii, Y., Good, S., Guinehut, S., Haines, K., Ishikawa, Y., Keeley, S., Köhl, A., Lee, T., Martin, M. J., Masina, S., Masuda, S., Meyssignac, B., Mogensen, K., Parent, L., Peterson, K. A., Tang, Y. M., Yin, Y., Vernieres, G., Wang, X., Waters, J., Wedd, R., Wang, O., Xue, Y., Chevallier, M., Lemieux, J.-F., Dupont, F., Kuragano, T., Kamachi, M., Awaji, T., Caltabiano, A., Wilmer-Becker, K., and Gaillard, F.: The Ocean Reanalyses Intercomparison Project (ORA-IP), J. Oper. Oceanogr., 8, s80–s97, https://doi.org/10.1080/1755876X.2015.1022329, 2015.

Behnisch, M., Macrander, A., Boebel, O., Wolff, J. O., and Schröter, J.: Barotropic and deep-referenced baroclinic SSH variability derived from pressure inverted echo sounders (PIES) south of Africa, J. Geophys. Res.-Oceans, 118, 3046–3058, https://doi.org/10.1002/jgrc.20233, 2013.

Chassignet, E. P., Hurlburt, H. E., Metzger, E. J., Smedstad, O. M., Cummings, J. A., Halliwell, G. R., Bleck, R., Baraille, R., Wallcraft, A. J., Lozano, C., Tolman, H. L., Srinivasan, A., Hankin, S., Cornillon, P., Weisberg, R., Barth, A., He, R., Werner, F., and Wilkin, J.: US GODAE: global ocean prediction with the HYbrid Coordinate Ocean Model (HYCOM), Oceanography, 22, 64–75, https://doi.org/10.5670/oceanog.2009.39, 2009.

Copernicus Marine Service (CMEMS): Global Ocean physics reanalysis, CMEMS Marine Data Store (MDS) [data set], https://doi.org/10.48670/moi-00021, 2018.

Copernicus Marine Service (CMEMS): Global Ocean gridded L4 sea surface heights and derived variables reprocessed 1993 ongoing, CMEMS Marine Data Store (MDS) [data set], https://doi.org/10.48670/moi-00148, 2025.

https://doi.org/10.5194/egusphere-2026-5239
Preprint. Discussion started: 9 September 2026

Copernicus Marine Service (CMEMS): Quality information document for sea level SLA products, CMEMS-SL-QUID-008-033-068, https://documentation.marine.copernicus.eu/QUID/CMEMS-SL-QUID-008-033-068.pdf (last access: 13 August 2026), 2026.

Cummings, J. A.: Operational multivariate ocean data assimilation, Q. J. Roy. Meteor. Soc., 131, 3583–3604, https://doi.org/10.1256/qj.05.105, 2005.

Dibarboure, G., Boy, F., Desjonqueres, J. D., Labroue, S., Lasne, Y., Picot, N., Poisson, J. C., and Thibaut, P.: Investigating short-wavelength correlated errors on low-resolution mode altimetry, J. Atmos. Ocean. Technol., 31, 1337–1362, https://doi.org/10.1175/JTECH-D-13-00081.1, 2014.

Donohue, K. A., Kennelly, M. A., and Cutting, A.: Sea surface height variability in Drake Passage, J. Atmos. Ocean. Technol., 33, 669–683, https://doi.org/10.1175/JTECH-D-15-0249.1, 2016.

Hallberg, R.: A thermobaric instability of Lagrangian vertical coordinate ocean models, Ocean Model., 8, 279–300, https://doi.org/10.1016/j.ocemod.2004.01.001, 2005.

Huang, Y., Zhang, L., Wang, F., Wang, F., and Hu, D.: Interannual variations of the North Equatorial Current/Undercurrent from mooring array observations, Front. Mar. Sci., 9, 979442, https://doi.org/10.3389/fmars.2022.979442, 2022.

Hwang, C., Min, H. S., Jeon, C., Kim, D. G., and Park, J.-H.: Estimation of sea surface height using pressure-recording inverted echo sounders data in the Mindanao Current region, Ocean Polar Res., 43, 219–227, https://doi.org/10.4217/OPR.2021.43.4.219, 2021.

HYCOM Consortium: GLBv0.08 Expt 53.X, https://www.hycom.org/data/glbv0pt08/expt-53ptx (last access: 16 August 2026), 2026.

Jeon, C., Park, J.-H., Kim, D. G., Kim, E., and Jeon, D.: Comparison of measurements from pressure-recording inverted echo sounders and satellite altimetry in the North Equatorial Current region of the western Pacific, Ocean Sci. J., 53, 207–213, https://doi.org/10.1007/s12601-018-0012-4, 2018.

Jeon, C., Watts, D. R., Min, H. S., Kim, D. G., Kang, S. K., Moon, I. J., and Park, J.-H.: Weakening of the Kuroshio upstream by cyclonic cold eddies enhanced by the consecutive passages of Typhoons Danas, Wipha, and Francisco (2013), Front. Mar. Sci., 9, 884768, https://doi.org/10.3389/fmars.2022.884768, 2022.

Jeon, C., Lee, K.-N., Song, H., Chae, J.-Y., and Park, J.-H.: Present and prospect of ocean observation using pressure-recording inverted echo sounder (PIES), J. Korean Soc. Oceanogr., 28, 51–61, https://doi.org/10.7850/jkso.2023.28.1.051, 2023.

Jeon, D. and Azminuddin, F.: POSEIDON_ADCP/RCM_CTD, Zenodo [data set], https://doi.org/10.5281/zenodo.1228158, 2018.

Kobashi, F. and Kawamura, H.: Seasonal variation and instability nature of the North Pacific Subtropical Countercurrent and the Hawaiian Lee Countercurrent, J. Geophys. Res., 107, 3185, https://doi.org/10.1029/2001JC001225, 2002.

Kobashi, F., Mitsudera, H., and Xie, S.-P.: Three subtropical fronts in the North Pacific: Observational evidence for mode water-induced subsurface frontogenesis, J. Geophys. Res., 111, C09033, https://doi.org/10.1029/2006JC003479, 2006.

https://doi.org/10.5194/egusphere-2026-5239
Preprint. Discussion started: 9 September 2026

Lellouche, J.-M., Greiner, E., Le Galloudec, O., Garric, G., Regnier, C., Drevillon, M., Benkiran, M., Testut, C.-E., Bourdalle-Badie, R., Gasparin, F., Hernandez, O., Levier, B., Drillet, Y., Remy, E., and Le Traon, P.-Y.: Recent updates to the Copernicus Marine Service global ocean monitoring and forecasting real-time 1/12° high-resolution system, Ocean Sci., 14, 1093–1126, https://doi.org/10.5194/os-14-1093-2018, 2018.

Lellouche, J.-M., Greiner, E., Bourdalle-Badie, R., Garric, G., Melet, A., Drévillon, M., Bricaud, C., Hamon, M., Le Galloudec, O., Regnier, C., Candela, T., Testut, C.-E., Gasparin, F., Ruggiero, G., Benkiran, M., Drillet, Y., and Le Traon, P.-Y.: The Copernicus global 1/12° oceanic and sea ice GLORYS12 reanalysis, Front. Earth Sci., 9, 698876, https://doi.org/10.3389/feart.2021.698876, 2021.

Masina, S., Storto, A., Ferry, N., Valdivieso, M., Haines, K., Balmaseda, M., Zuo, H., Drevillon, M., and Parent, L.: An ensemble of eddy-permitting global ocean reanalyses from the MyOcean project, Clim. Dyn., 49, 813–841, https://doi.org/10.1007/s00382-015-2728-5, 2017.

Metzger, E. J., Helber, R. W., Hogan, P. J., Posey, P. G., Thoppil, P. G., Townsend, T. L., Wallcraft, A. J., Smedstad, O. M., Franklin, D. S., Zamudio-Lopez, L., and Phelps, M. W.: Global Ocean Forecast System 3.1 validation testing, Naval Research Laboratory, Oceanography Division, Stennis Space Center, MS, NRL/MR/7320--17-9722, 59 pp., https://www7320.nrlssc.navy.mil/pubs/2017/metzger-2017.pdf, 2017.

Park, J.-H., Watts, D. R., Donohue, K. A., and Tracey, K. L.: Comparisons of sea surface height variability observed by pressure-recording inverted echo sounders and satellite altimetry in the Kuroshio Extension, J. Oceanogr., 68, 401–416, https://doi.org/10.1007/s10872-012-0108-x, 2012.

Qiu, B.: Seasonal eddy field modulation of the North Pacific Subtropical Countercurrent: TOPEX/Poseidon observations and theory, J. Phys. Oceanogr., 29, 2471–2486, https://doi.org/10.1175/1520-0485(1999)029<2471:SEFMOT>2.0.CO;2, 1999.

Qiu, B., Rudnick, D. L., Chen, S., and Kashino, Y.: Quasi-stationary North Equatorial Undercurrent jets across the tropical North Pacific Ocean, Geophys. Res. Lett., 40, 2183–2187, https://doi.org/10.1002/grl.50394, 2013.

Qiu, B., Rudnick, D. L., Cerovecki, I., Cornuelle, B. D., Chen, S., Schönau, M. C., McClean, J. L., and Gopalakrishnan, G.: The Pacific North Equatorial Current: new insights from the origins of the Kuroshio and Mindanao Currents (OKMC) project, Oceanography, 28, 24–33, https://doi.org/10.5670/oceanog.2015.78, 2015.

Roemmich, D., Alford, M. H., Claustre, H., Johnson, K., King, B., Moum, J., Oke, P., Owens, W. B., Pouliquen, S., Purkey, S., Scanderbeg, M., Suga, T., Wijffels, S., Zilberman, N., Bakker, D., Baringer, M., Belbeoch, M., Bittig, H. C., Boss, E., Calil, P., Carse, F., Carval, T., Chai, F., Ó Conchubhair, D., d'Ortenzio, F., Dall'Olmo, G., Desbruyeres, D., Fennel, K., Fer, I., Ferrari, R., Forget, G., Freeland, H., Fujiki, T., Gehlen, M., Greenan, B., Hallberg, R., Hibiya, T., Hosoda, S., Jayne, S., Jochum, M., Johnson, G. C., Kang, K., Kolodziejczyk, N., Körtzinger, A., Le Traon, P.-Y., Lenn, Y.-D., Maze, G., Mork, K. A., Morris, T., Nagai, T., Nash, J., Naveira Garabato, A., Olsen, A., Pattabhi, R. R., Prakash, S., Riser, S., Schmechtig, C., Schmid, C., Shroyer, E., Sterl, A., Sutton, P., Talley, L., Tanhua, T., Thierry, V., Thomalla, S., Toole, J., Troisi, A., Trull, T. W., Turton, J., Velez-Belchi, P. J., Walczowski, W., Wang, H., Wanninkhof, R., Waterhouse, A. F., Waterman, S., Watson, A., Wilson,

https://doi.org/10.5194/egusphere-2026-5239
Preprint. Discussion started: 9 September 2026

C., Wong, A. P. S., Xu, J., and Yasuda, I.: On the future of Argo: a global, full-depth, multi-disciplinary array, Front. Mar. Sci., 6, 439, https://doi.org/10.3389/fmars.2019.00439, 2019.

Song, H., Zhu, X.-H., Zhu, Z.-N., Chae, J.-Y., Jeon, C., Kim, D.-G., Min, H.-S., Lee, J.-H., and Park, J.-H.: Seasonal variability of the deep western boundary current in the Philippine Sea, J. Mar. Sci. Eng., 11, 1290, https://doi.org/10.3390/jmse11071290, 2023.

Storto, A., Masina, S., Balmaseda, M., Guinehut, S., Xue, Y., Szekely, T., Fukumori, I., Forget, G., Chang, Y.-S., Good, S. A., Köhl, A., Vernieres, G., Ferry, N., Peterson, K. A., Behringer, D., Ishii, M., Masuda, S., Fujii, Y., Toyoda, T., Yin, Y., Valdivieso, M., Barnier, B., Boyer, T., Lee, T., Gourrion, J., Wang, O., Heimbach, P., Rosati, A., Kovach, R., Hernandez, F., Martin, M. J., Kamachi, M., Kuragano, T., Mogensen, K., Alves, O., Haines, K., and Wang, X.: Steric sea level variability (1993–2010) in an ensemble of ocean reanalyses and objective analyses, Clim. Dyn., 49, 709–729, https://doi.org/10.1007/s00382-015-2554-9, 2017.

Storto, A., Alvera-Azcárate, A., Balmaseda, M. A., Barth, A., Chevallier, M., Counillon, F., Domingues, C. M., Drevillon, M., Drillet, Y., Forget, G., Garric, G., Haines, K., Hernandez, F., Iovino, D., Jackson, L. C., Lellouche, J.-M., Masina, S., Mayer, M., Oke, P. R., Penny, S. G., Peterson, K. A., Yang, C., and Zuo, H.: Ocean reanalyses: recent advances and unsolved challenges, Front. Mar. Sci., 6, 418, https://doi.org/10.3389/fmars.2019.00418, 2019.

Verezemskaya, P., Barnier, B., Gulev, S. K., Gladyshev, S., Molines, J.-M., Gladyshev, V., Lellouche, J.-M., and Gavrikov, A.: Assessing eddying (1/12°) ocean reanalysis GLORYS12 using the 14-yr instrumental record from 59.5°N section in the Atlantic, J. Geophys. Res.-Oceans, 126, e2020JC016317, https://doi.org/10.1029/2020JC016317, 2021.

Watts, D. R. and Rossby, H. T.: Measuring dynamic heights with inverted echo sounders: results from MODE, J. Phys. Oceanogr., 7, 345–358, https://doi.org/10.1175/1520-0485(1977)007<0345:MDHWIE>2.0.CO;2, 1977.

Xia, Q., Li, G., and Dong, C.: Global oceanic mass transport by coherent eddies, J. Phys. Oceanogr., 52, 1111–1132, https://doi.org/10.1175/JPO-D-21-0103.1, 2022.

Zhang, L., Wang, F. J., Wang, Q., Hu, S., Wang, F., and Hu, D.: Structure and variability of the North Equatorial Current/Undercurrent from mooring measurements at 130°E in the western Pacific, Sci. Rep., 7, 46310, https://doi.org/10.1038/srep46310, 2017.

Zhong, Y., Zhou, M., Waniek, J. J., Zhou, L., and Zhang, Z. R.: Seasonal variation of the surface Kuroshio intrusion into the South China Sea evidenced by satellite geostrophic streamlines, J. Phys. Oceanogr., 51, 2705–2718, https://doi.org/10.1175/JPO-D-20-0242.1, 2021.